Pressure-induced loss of metallicity in RuO_2

Melanie White,[1,2] Daniel Schacher,[1,2] G. Alexander Smith,[1,3] Dean Smith,[1] Changyong Park,[4] Keith V. Lawler,[1,*] and Ashkan Salamat[1,2,†]

[1]*Nevada Extreme Conditions Laboratory, University of Nevada, Las Vegas, Las Vegas, Nevada 89154, USA*
[2]*Department of Physics & Astronomy, University of Nevada Las Vegas, Las Vegas, Nevada 89154, USA*
[3]*Department of Chemistry & Biochemistry, University of Nevada Las Vegas, Las Vegas, Nevada 89154, USA*
[4]*HPCAT, X-ray Science Division, Argonne National Laboratory, Argonne, Illinois 60439, USA*

(Received 7 July 2023; accepted 12 December 2023; published 16 January 2024)

The density evolution of the physical properties of the transition-metal oxide RuO_2 coupled with a deeper understanding of underlying metastable phases is necessary for correlating universality between similar binary systems. Here, we report the pressure-temperature electrical resistance dependency with the structural evolution of RuO_2. Conducting quasi-four-probe electrical transport measurements in a diamond anvil cell, a low-temperature loss of metallicity is observed above 28 GPa. This insulative transition is accompanied by a significant drop in pressure, suggesting the electronic transition is linked to a first-order structural phase transition. This is supported by the observation that the insulative electronic state is retained upon warming to room temperature. Density functional theory simulations indicate that the insulative fluorite-type phase can be favorable around these conditions and would exhibit a similar pressure difference through an isochoric transformation from the metallic HP-PdF_2-type phase, however there is insufficient experimental evidence to confirm the presence of the fluorite-type phase. Furthermore, a unique arsenopyrite-type phase of RuO_2 is observed with x-ray diffraction of a post-laser-heated sample at 62 GPa.

DOI: 10.1103/PhysRevMaterials.8.013603

I. INTRODUCTION

Transition-metal oxides are valued for their rich variety of electronic properties facilitated by the presence of d-orbital interactions [1,2]. Examples include metal-insulator transitions like those found in NbO_2 and VO_2 [3–5] and intrinsic magnetic semiconductivity in spintronic materials MnO_2 and TcO_2 [6,7]. The d-orbital interactions can also be tuned via chemical or mechanical means to modify these electronic properties, the possibilities of which have been embraced by the high-pressure community. In this work, we focus on RuO_2, a $4d$ transition-metal oxide and gold-standard electrocatalyst used in numerous industrial processes such as converting CO to CO_2, producing Cl_2 gas and NaOH from salt water, and splitting water to form molecular H_2 [8]. The addition of structural strain reveals more characteristics of RuO_2, such as the enhancement of catalytic efficiency through strain engineering [9], strain-induced superconductivity in thin films [10], and metal-insulator transitions (MITs) in low-dimensional, highly disordered systems [11–13].

The ground-state assembly for RuO_2 is the rutile-type ($P4_2/mnm$) structure, a common polymorph of transition-metal dioxides. In a reported range of 5–12 GPa, RuO_2 undergoes a second-order transition from a rutile-type to $CaCl_2$-type ($Pnnm$) structure [14–17], a phase progression shared by other prominent metal binary oxides such as the geologically abundant stishovite [18]. Recent work on group 14 oxides SnO_2 and GeO_2 probed oxygen sublattice disordering preceding rutile-$CaCl_2$ transitions, which in SnO_2 presented with orders of magnitude (10^4) reduction in electrical resistance [19,20]. The driving mechanism behind the disordering and transition is postulated to be universal for MO_2 rutile-$CaCl_2$ transitions, and as such the electrical performance of isostructural d-block oxides across the same transition is of interest [19,20].

Following the $CaCl_2$-type phase, RuO_2 undergoes a first-order transition to a HP-PdF_2-type ($Pa\bar{3}$) structure in a range of 11–30 GPa, with the two phases coexisting to at least ≈50 GPa, the highest pressure explored experimentally prior to this work [14,16,17,21–23]. Historically, the $Pa\bar{3}$ phase of RuO_2 has been described as a pyrite-type or modified fluorite structure [17,18,22,24–26]. However, since $Pa\bar{3}$ RuO_2 lacks the anion-anion bonding of a pyrite-type material, it is better described by the high-pressure cubic phase of PdF_2, which is crystallographically identical to the pyrite structure without anion-anion bonds [27,28]. In several studies, the $Pa\bar{3}$ phase was not observed, which in combination with phase coexistence suggests phase metastability, slow kinetics of formation, and possibly a high sensitivity to sample environment and conditions of formation [15–17,29]. Previously, the $Pa\bar{3}$ phase was of considerable interest due to having a bulk modulus near that of diamond, though it has been subsequently ruled out as a potential superhard material [14,30–32]. Computational studies exploring possible other phases above 50 GPa have determined a fluorite-type (CaF_2-type, $Fm\bar{3}m$) structure to be energetically favorable [18,26,32]. The transition to $Fm\bar{3}m$

*keith.lawler@unlv.edu
†ashkan.salamat@unlv.edu

would also be accompanied by an MIT, as density-of-states (DOS) calculations indicate the fluorite-type phase is an insulator while the rutile-type, $CaCl_2$-type, and HP-PdF_2-type are either known or predicted to be metallic [25,33–35].

Here, we probe the phase progression and phase properties of RuO_2 with a combination of electrical resistance measurements and synchrotron x-ray diffraction (XRD), finding that certain thermodynamic pathways can elicit an insulative transition in RuO_2 and access new high-pressure phases.

II. METHODS

All high-pressure measurements were carried out in custom diamond anvil cells (DACs). RuO_2 powder was purchased from Sigma Aldrich, 99.9% trace metal basis. For transport measurements on microscale samples, electrical contacts were cut from 4 μm thickness Pt foil. Metal gaskets were electrically insulated from the Pt probes with a layer of Al_2O_3 powder mixed with approximately 8% by weight Stycast 1266. The insulating layer acted as the *de facto* pressure-transmitting medium. Pressures were calculated from ruby spheres loaded adjacent to samples or using the Raman spectra of the center of the diamond culet [36,37].

For low-temperature measurements specifically, we employ the ruby fluorescence pressure scale created by Feng *et al.* [38]. Our values for the Feng variable $\lambda_0(T)$ were estimated by applying the temperature corrections of Datchi *et al.* [39] to the room-temperature, pre-compression λ_0 of our ruby manometers. Of the different low-temperature ruby scales in the literature [38–41], we found this scale provided the best consistency between our ruby and diamond pressures in data sets where both quantities were measured.

A Cryomech ST405 cryostat with optical access was utilized for low-temperature measurements. We had *in situ* pressure determination for four of the five low-temperature experiments detailed in this work. Temperatures in the cryostat were cycled twice between 9 and 185 K, with electrical and pressure measurements collected during the "warm-up" portion of each cycle. Above 185 K, we found our cryostat system had limited temperature control capabilities, and as such we only present with confidence the data in the temperature range 9–185 K.

Synchrotron angular dispersive XRD measurements of RuO_2 were carried out using two different types of DAC loadings. The first was a DAC prepared for electrical transport measurements as described above. The second was a DAC prepared for laser heating as follows: RuO_2 powder was placed on a platform of NaCl pellets and gas-loaded with argon as a pressure transmitting medium (PTM) using an in-house gas loader [42]. RuO_2 was compressed to 64 GPa, as determined by diamond culet Raman spectra, and laser-annealed in-house using an IPG YLF ($\lambda = 1070$ nm) laser. Experiments were conducted at HPCAT, 16 ID-B, and BM-D beamlines of the Advanced Photon Source with $\lambda = 0.4066$ and 0.4133 Å, respectively. Diffraction was performed axially through the diamond anvil using Boehler-Almax conical design diamonds to allow for a 70° solid angle aperture. Pressures were determined using the equation of state (EOS) of platinum, in the case of the transport cell, and of argon for the laser-annealed cell [43,44]. Diffraction data were integrated using DIOPTAS software, and structural analysis was performed using GSAS-II software [45,46].

Ab initio density functional theory (DFT) utilizing VASP (Vienna ab initio simulation package) 5.4 was used for structural minimization and calculation of the electronic ground state and phonons at varying pressures. Vibrational free-energy contributions within the harmonic approximation were calculated using PHONOPY [47,48]. The strongly constrained and appropriately normed (SCAN) meta-GGA (generalized gradient approximation) functional was used throughout all calculations [49]. A Γ-centered k-point grid with 0.15 Å^{-1} spacing was used in each calculation. Gaussian smearing with a width of 0.10 eV was used to determine partial occupancies [50]. The VASP projector-augmented wave (PAW) pseudopotentials were used for both Ru and O with a valence configuration of $4s^24p^65s^24d^6$ and $2s^22p^4$, respectively [51]. The energy and force convergence parameters were set to at least a difference of 10^{-8} eV and 10^{-3} eVÅ^{-1}, respectively. Structural optimizations were performed as a series of two sequential ionic optimizations followed by a final evaluation of the ground-state energy. Crystal structure prediction (CSP) simulations were performed using the evolutionary algorithm of the USPEX package [52–54]. Each predicted crystal structure was optimized twice (once relaxing the cell shape and volume and once relaxing all parameters) with the SCAN functional in VASP. The CSP optimizations used a coarser $0.05 \times 2\pi$ Å^{-1} k-grid as well as a smaller Mn PAW pseudopotential with a valence configuration $4p^65s^24d^6$ (i.e., "Mn_pv" instead of "Mn_sv").

III. RESULTS AND DISCUSSION

The results of low-temperature, high-pressure electrical transport measurements are shown in Fig. 1. The DACs were pressurized to different starting pressures prior to being situated in the cryostat system. Measurements for the 16, 28, and 42 GPa series were done with the same DAC loading, while the 36 and 60 GPa series were separate loadings. In all five cases, the initial sample resistance prior to cooling was on the order of 3–6 Ω. For the average pressures of 16 and 28 GPa, the RuO_2 sample resistance exhibits a typical temperature response for metals, and it appears to be becoming less metallic with increasing pressure. We see a dramatic increase of approximately three orders of magnitude in electrical resistance for the experiments with average pressures of 36, 42, and 60 GPa. This indicates a possible metal-insulator transition, though semimetals and semiconductors can exhibit similar low-temperature behavior, especially if the concentration of charge carriers is small [55]. The varying degrees of coexistence of the $CaCl_2$-type and HP-PdF_2-type phases over these pressures further complicates analysis. We found that the transition was not necessarily immediate or stable upon cooling, as seen in Figs. 1 and 2, suggesting some pressure and temperature cycling may be needed to promote or fully complete the transition. Once transformed, the sample remained in the insulator-like state through the rest of the first and entirety of the second temperature cycles. With separate DAC loadings, the lower magnitude of resistance values at 42 GPa compared to 36 and 60 GPa cannot be directly interpreted as changes in electrical performance between these pressures.

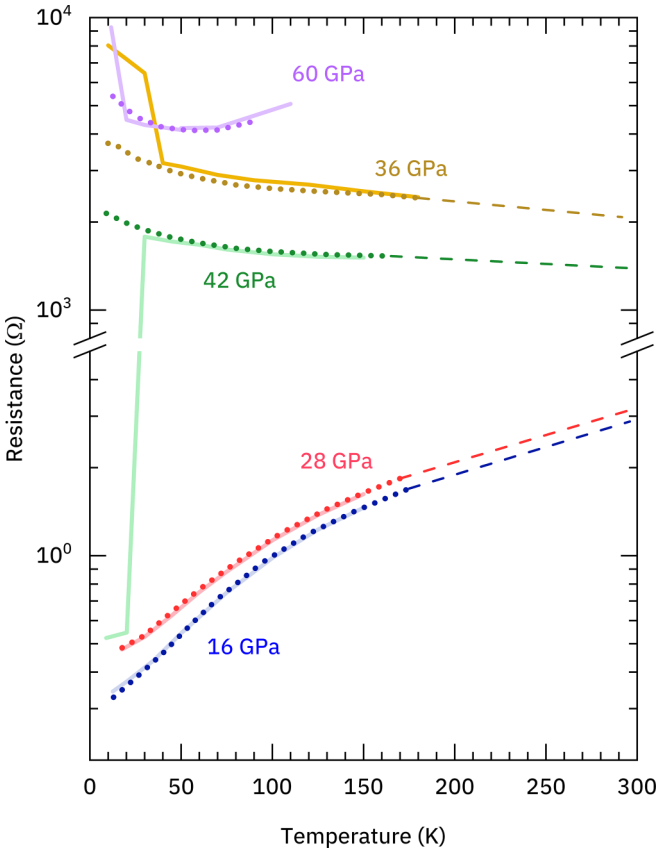

FIG. 1. Temperature-dependent electrical transport measurements made at five pressure ranges reveal a significant change in the electronic property of RuO_2 occurring between 28 and 36 GPa. The data are color-coded and labeled based on the average value of measured pressures collected before, after, and during the dual "warm-up" cycles. Solid lines depict the first cycle and dotted lines the second cycle in the range of approximately 9–185 K. Dashed lines in the 16, 28, 36, and 42 GPa series extrapolate from the final low-temperature measurement to the sample resistance after the system has warmed back to ≈300 K. Room-temperature resistance was not available at the end of the 60 GPa series.

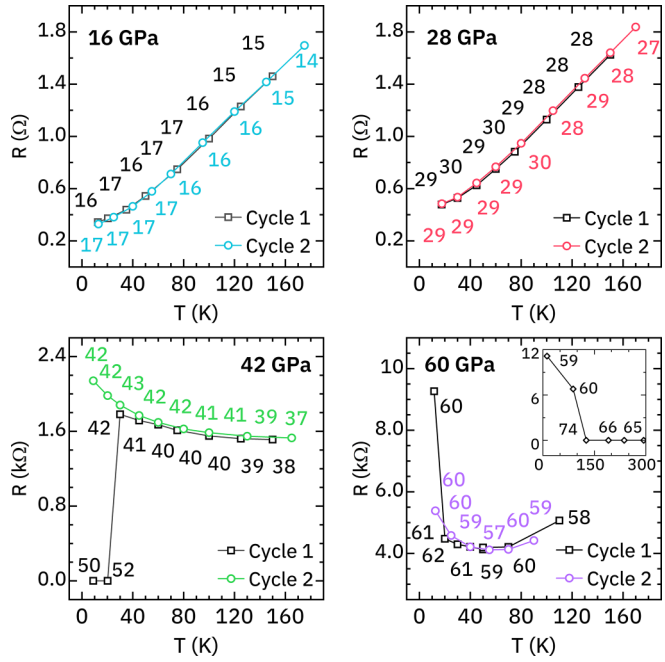

FIG. 2. Associated pressures for the resistance-temperature data of Fig. 1, not including initial and final room-temperature points. Changes in temperatures cause thermal expansion or contraction in the DAC and cryostat assembly, resulting in pressure changes throughout the warming and cooling cycles. To monitor this, pressure was measured at 10–25 K temperature intervals while warming over the range of 9–185 K. The inset in the 60 GPa plot includes data from the initial cool-down of the cryostat, which captured the dramatic change in resistance and simultaneous decrease in pressure. *In situ* pressure measurements were not available during the 36 GPa cycles.

Interestingly, the electronic transition is not immediately reversible upon warming to room temperature, and sample resistance remains in the kΩ regime. We did observe electrical resistance in the 36 and 42 GPa DAC loadings decreased post-transformation after the DACs had rested awhile at room temperature. Resistance in the post-transformed 36 GPa sample decreased by 600 Ω over the period of 6 months, while the 42 GPa sample decreased by 130 Ω over 1 month. This could indicate that transformed RuO_2 will slowly convert back to its pre-transition, more metallic state if continually stored at room temperature. We do not have data of the post-transform room-temperature electrical response for the 60 GPa loading. The persistent nature of this loss in metallicity even at room temperature suggests that exposure to low temperatures resulted in a change to the RuO_2 crystal lattice, such as a strong lattice structural distortion or a transition to a new phase, that has a costly kinetic barrier preventing back-transformation.

The three high-pressure series that exhibit the increases in electrical resistance also experienced uncharacteristically large drops in pressure. This is captured at 42 GPa in Fig. 2, which shows a ≈10 GPa drop in pressure coinciding with the change from roughly 3 Ω to 1.8 kΩ. After this transition, values of pressure are more smoothly varying, and differences between points are relatively small (within a few gigapascals). Unlike the 42 GPa warm-up cycle, the electrical transitions for the other two series occurred during the initial cryostat cool-down, in the case of 60 GPa, or while reaching thermal equilibrium prior to the first warm-up cycle, in the case of 36 GPa. Thus, the small increase in temperature preceding the electrical transition in the first warm-up cycle of the 42 GPa series is not required for the transformation; rather, the delay is likely sluggish kinetics due to the low temperatures. Variation between samples and nonhydrostatic sample environments may be additional contributing factors to variation in transition behavior, on top of the changing relative percentages of $CaCl_2$-type and HP-PdF_2-type phases across our experimental pressure range. At 60 GPa in Fig. 2, a nearly 10 kΩ increase in resistance was accompanied by a 14 GPa decrease in pressure (shown in the inset). *In situ* pressure measurements were not possible in the case of the 36 GPa series, which experienced a ≈2.3 kΩ increase in resistance; however, pressure measurements before and after the cryostat experiment revealed an overall decrease of approximately 13 GPa.

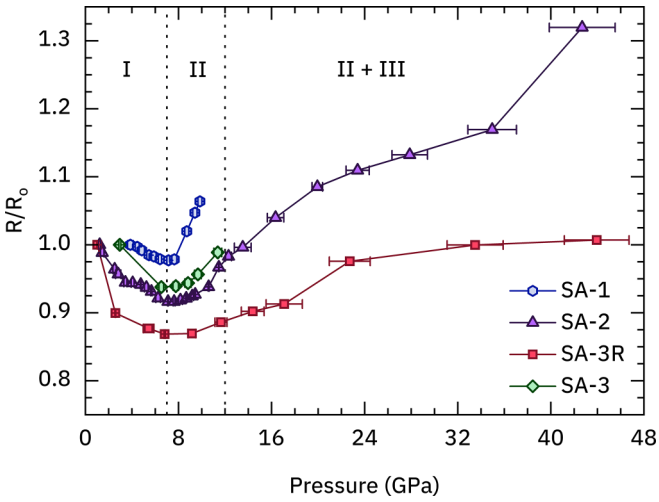

FIG. 3. Comparison of electrical resistance as a function of pressure from four separate DAC loadings at room temperature. Each series is scaled by the initial resistance of their first pressure point. Phase boundaries are approximated by vertical dotted lines to guide the eye and labeled with Roman numerals, with phase I indicating the rutile-type phase, phase II the $CaCl_2$-type phase, and phase II + III the regime where the HP-PdF_2-type phase reportedly emerges but coexists with the $CaCl_2$-type phase [17]. Data are labeled with the simple code names used for each DAC during experiments.

In contrast, such pressure drops are not seen in the two series at 16 and 28 GPa, which exhibit the more common behavior of smoothly increasing pressure as temperature decreases, and vice versa. Sudden jumps in pressure on the order of what we observe in the three series at 36, 42, and 60 GPa are not typical. Rather, they are suggestive of the pressure drops one often observes in high-pressure experiments when samples undergo first-order phase transitions. Further details of pressure, temperature, and electrical resistance during these experiments are provided in [56].

Data from four separate room-temperature compression experiments are combined in Fig. 3, each set scaled by the resistance value of the initial pressure point so that measurements from separate loadings may be viewed and compared on the same scale. They show changes in resistance trends that correlate well with pressures where structural phase transitions are known to occur, marked by vertical dotted lines at 7 and 12 GPa for the $CaCl_2$-type and HP-PdF_2-type phase boundaries, respectively [17]. The metallicity of RuO_2 improves upon application of pressure while in the rutile-type phase, but worsens in the $CaCl_2$-type and HP-PdF_2-type phases. In series with a high density of points, we observe slight but measurable resistance changes between 3 and 6 GPa that could be linked to anion disordering preceding the rutile-type to $CaCl_2$-type transition that we observe between 6.3 and 7.8 GPa (see the Supplemental Material [56]). The possible disordering does not result in an orders-of-magnitude change in electrical resistance at room temperature, such as the kind seen in SnO_2, likely due to the metallic nature of both rutile-type and $CaCl_2$-type phases of RuO_2 [19,20]. As none of the room-temperature measurements acquired up to ≈44 GPa exhibit the same electronic transition as their cryogenically cooled counterparts, low temperatures appear to be required in addition to pressure to access the state experimentally.

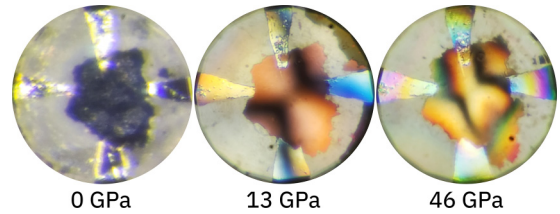

FIG. 4. Microscope images of RuO_2 in a DAC prepared for electrical transport measurements. Increasing pressure reveals an evolution in color from near-black to predominately yellow. The sample sits atop a white semitransparent layer of Al_2O_3 + Stycast 1226 mixture and four platinum probes. Images were acquired at room temperature.

Figure 4 reveals the color evolution of metallic RuO_2 as pressure increases at room temperature. Micrographs were acquired in reflection geometry using polychromatic light. At ambient conditions RuO_2 appears dark gray, close to black. A color change to a reddish hue is observed starting at 3 GPa; such a color change for rutile-type RuO_2 has been noted in previous reports [14,15]. The reddish hue is still visible here at 13 GPa. By 22 GPa, yellow emerges and becomes the increasingly dominant color, as seen in the image at 46 GPa. Color changes can indicate changes in the electronic structure of a material. Rosenblum *et al.* [15] posits that the color change from black to red relates to a small pressure-induced shift in the optical constants, especially with regard to the sharp minimum near 2 eV in ambient rutile-type RuO_2's reflectivity spectrum [33,57]. The yellow coloration is likely a continuation of this trend with respect to pressure.

Figure 5 displays our enthalpy calculations for the three established phases of RuO_2 as a function of pressure, with the addition of fluorite-type and arsenopyrite-type RuO_2, two phases we hypothesize may be formed under specific conditions. When compared with the phase boundaries shown in

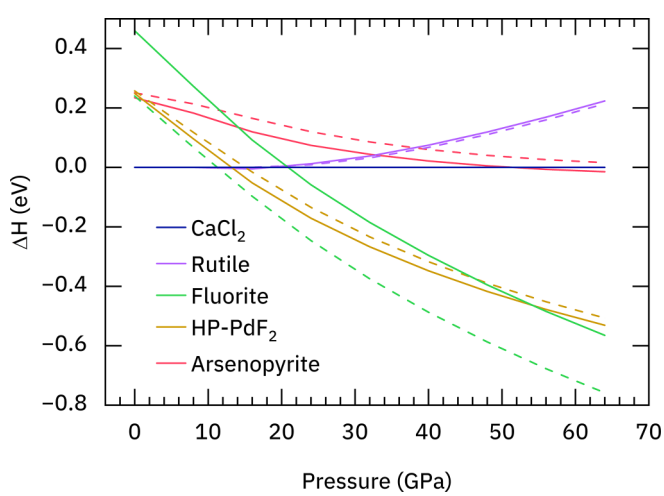

FIG. 5. Enthalpy as a function of pressure up to 64 GPa using the SCAN (solid) or SCAN+U_{eff} = 1.25 eV (dashed) functional for candidate structures of high-pressure RuO_2, relative to the $CaCl_2$-type phase.

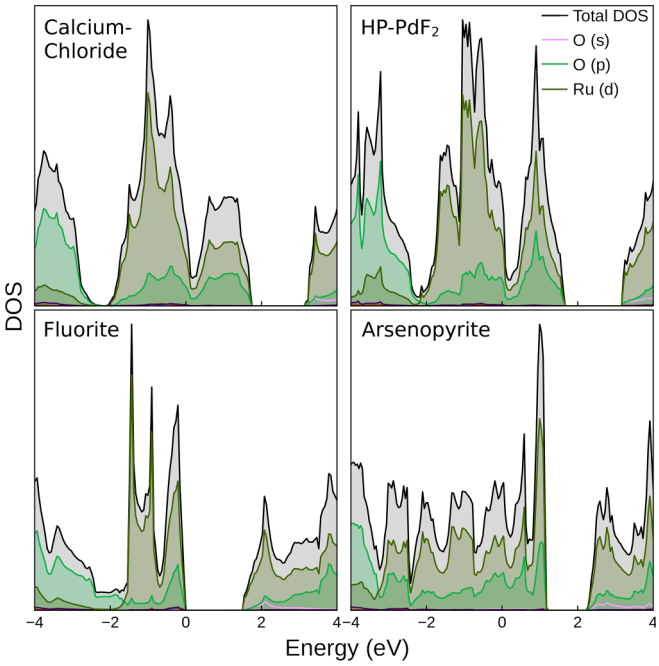

FIG. 6. Electronic density of states for 40 GPa $CaCl_2$-type, HP-PdF_2-type, fluorite-type, and arsenopyrite-type RuO_2. Out of all the candidate structures, the fluorite phase is the only nonmetallic phase with a band gap of 1.494 eV.

Fig. 3, our enthalpy calculations show that the $CaCl_2$-type phase begins to distinguish itself from the rutile-type phase around 8 GPa, and by 14 GPa the HP-PdF_2-type is the most enthalpically favorable phase. Our calculations suggest that fluorite-type RuO_2 ultimately becomes the most favorable structure under sufficiently high pressures. When vibrational energy contributions are not considered, the fluorite-type phase does not overtake the HP-PdF_2-type phase as the most enthalpically favorable until 55 GPa, implying that the phases observed in the 16, 28, 36, and 42 GPa series of resistance measurements should be confined to the rutile-type, $CaCl_2$-type, and HP-PdF_2-type structures (although the range of pressures experienced within the 36 GPa series is unknown). In agreement with prior calculations [25], the rutile-type, $CaCl_2$-type, and HP-PdF_2-type phases are all predicted here to be metallic; selected partial electronic densities of states are included in Fig. 6. The density of states at the Fermi level, $N(\epsilon_f)$, in both the $CaCl_2$-type and HP-PdF_2-type phases tends to decrease monotonically as a function of pressure: from 0 to 48 GPa the HP-PdF_2-type phase goes from 1.675 to 1.393 states/eV/formula unit, and the $CaCl_2$-type phase from 1.289 to 1.222 states/eV/formula unit.

The metallic nature of the most favorable phases below 55 GPa does not offer an explanation for the low-temperature increase in resistance observed above 28 GPa, even considering that over the investigated pressure range the sample is expected to contain combinations of $CaCl_2$-type and HP-PdF_2-type phases. We examined RuO_2 in the form of different common MO_2 polymorphs to investigate if a new phase could account for the loss of metallicity. Of the structures evaluated, only the fluorite-type structure was found to have an energy band gap at the Fermi level in the same pressure regime of the low-temperature resistance measurements. The reason for this can be explained according to crystal-field theory, whereby the Ru^{4+} ion with four localized d electrons should prefer a low spin ($S = 0$) coordination wherein the e_g states are fully occupied and the t_{2g} are fully unoccupied (i.e., like a tetrahedral coordination). This is opposed to the distorted octahedral coordination of the rutile-type, $CaCl_2$-type, and HP-PdF_2-type phases; this coordination leads to metallic Ru d (t_{2g}) states hybridized with O p states that span the Fermi level. Examination of the electron localization function (ELF) of both the HP-PdF_2-type and fluorite-type phases reveals a shift in the concentration of electrons around the Ru ion indicative of the change in crystal-field splitting from an octahedral complex in the rutile-type, $CaCl_2$-type, and HP-PdF_2-type phases to a tetrahedral complex in the fluorite-type phase (see the plots in the Supplemental Material [56]).

Crystal structure prediction (CSP) of 50 GPa RuO_2 with 1–4 formula units was employed to determine if any other candidate phases of RuO_2 exist that could cause the resistance behavior illustrated in Figs. 1 and 2. The known RuO_2 structures as well as other known high-pressure structural archetypes for AX_2 systems (including marcasite, cottunite, orthorhombic-ZrO_2, α-PbO_2, baddeleyite, arsenopyrite, monoclinic-VO_2, MoO_2, and monoclinic-distorted rutile [4,58–62]) were seeded into the CSP simulation. The lowest enthalpy structure found was the fluorite structure, beating the seeded HP-PdF_2 structure by 6 meV/formula units. The preference for the fluorite structure was found to be a consequence of k-grid convergence, as reevaluation of the energetics of the CSP optimized structures on a denser k-grid found an energy ordering like that shown in Fig. 5. All of the structures predicted within 100 meV/atom of the lowest enthalpy structure optimized to a slightly distorted version of either the fluorite-type of HP-PdF_2-type structures. The enthalpy versus pressure curves for the lowest enthalpy distorted HP-PdF_2-type (identified as space group $Pbc2_1$) and the only distorted fluorite-type that was not identified by USPEX as being $Fm\bar{3}m$ (identified as $C2/m$) closely follow those of the parent structures (see Fig. S11 in [56]) implying the residual distortions were again an artifact of the coarse-graining used for the CSP calculations. Likewise, their electronic properties mimic those of the parent structures with the $Pbc2_1$ structure being metallic and the $C2/m$ structure having a computed band gap of 1.49 eV.

Beyond the "0 K" enthalpies shown in Fig. 5, the inclusions of thermal vibrational energy contributions do not cause the insulating fluorite-type phase to overtake the favorability of the HP-PdF_2-type phase at an intermediate pressure of 40 GPa. However, if the simulations are performed isochorically instead of isobarically, then a different picture emerges. A setup similar to the quasiharmonic approximation was employed to make isochoric comparisons, wherein the target fluorite-type phase was optimized as a function of pressure and the HP-PdF_2-type phase was evaluated at the same volumes as determined for the target fluorite-type phase. Despite both phases having similar cubic structures, the fluorite phase was found to be significantly denser. This amounts to an external 12–14 GPa worth of pressure needing to be applied to the HP-PdF_2-type structure to have it be isochoric with the fluorite-type structure in the pressure range of 40–64 GPa,

for example. This is precisely the range of pressure differences observed when the higher resistance state is accessed, such as the cases of the 42 and 60 GPa series in Fig. 2. Within this isochoric comparison, the fluorite-type phase is more energetically favorable than the HP-PdF_2-type phase at lower temperatures, i.e., from 0 to 550 K in the volume of 46 GPa fluorite-type RuO_2. Even when analyzed isobarically at pressures where the fluorite phase is the most favorable according to Fig. 5, the HP-PdF_2-type phase will become more energetically favorable at a sufficiently high temperature, i.e., by 770 K at 64 GPa. Thus, the fluorite-type phase can be viewed as a possible low-temperature phase of RuO_2 in the pressure region around the electronic transition. Based on these calculations, one hypothesis for what is occurring is that during the low-temperature measurements, the oxygens of HP-PdF_2-type RuO_2 shift to the more highly symmetric positions of fluorite-type RuO_2, resulting in the observed drop in pressure and corresponding increase in electrical resistance.

It has been recently observed that RuO_2 exhibits itinerant antiferromagnetism at ambient conditions, evolving the long-held understanding of the material as a simple paramagnet [63]. The SCAN functional alone does not predict the ambient rutile-type phase of RuO_2 to be an antiferromagnet, and DFT+U using the single-parameter U_{eff} formulation [64] with a U_{eff} of 1.25 eV is required to reproduce the experimental magnetic moment ($0.05\mu_B$) [63]. Both the 0 GPa rutile-type and $CaCl_2$-type RuO_2 exhibited antiferromagnetic ordering when treated with DFT+U. Only at 32 GPa does the nonmagnetic state energetically overtake the antiferromagnetically ordered state of those structural phases. However, inspection of the partial density of states of the magnetically ordered states reveals them to be (semi)metallic up to 32 GPa just like their nonmagnetic counterparts. Likewise, no such magnetic ordering could be found for the HP-PdF_2-type phase, dictating that magnetic ordering is not responsible for the low-temperature change in resistance observed above 28 GPa.

Using the same empirically determined U_{eff} of 1.25 eV causes the fluorite-type phase to be more enthalpically favorable than the HP-PdF_2-type phase across the entire 0–64 GPa pressure range considered, as shown in Fig. 5. The transition pressure from the $CaCl_2$-type phase into the fluorite-type phase with DFT+U is around 11 GPa. DFT+U does increase the volumes of the optimized structures for the fluorite-type and HP-PdF_2-type phases relative to the calculations without the +U correction. However, the volume increase is minimal, and its magnitude decreases with pressure with the largest change being 0.293% in the ambient fluorite-type structure. The DFT+U P-V relationships indicate an 8–12 GPa pressure difference between the isochoric structures of the denser fluorite-type phase and the HP-PdF_2-type phase, which is still in line with the pressure drop observed along with the electronic transition. HP-PdF_2-type RuO_2 remains metallic with the +U correction applied, even with varying U_{eff} up to 6 eV (see the Supplemental Material [56]). In contrast, the fluorite-type phase remains insulative with the band gap increasing with the value of U_{eff}. This helps further rule out the possibility of a metal-to-insulator transition in the HP-PdF_2-type phase as an explanation for the loss of metallicity, and further supports the possibility of a low-temperature fluorite-type phase.

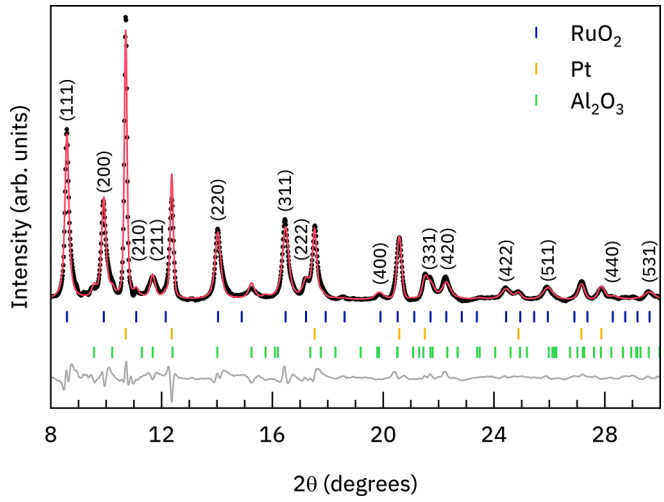

FIG. 7. Reitveld refinement (Rwp = 0.47%) of the HP-PdF_2-type structure to the XRD of RuO_2 at 43 GPa after being recovered from low-temperature experiments and transitioning to the high resistance state. The diffraction includes contributions from the Al_2O_3 mixture electrical insulation and Pt electrical leads. The magenta line is the Rietveld refinement of the $Pa\bar{3}$ structure to the raw data, marked by black circles, and the gray line is the difference between both. This plot has been background-subtracted; a version with the original background can be found in [56]. Nonzero intensity Bragg peaks of HP-PdF_2-type RuO_2 are identified with corresponding *hkl*s.

To evaluate the structure of this high-resistance state of RuO_2, the 60 GPa series DAC was examined using synchrotron XRD following the completion of low-temperature cryostat experiments. The evident persistence of the high resistance state of RuO_2 above cryogenic temperatures made us hopeful that a significant fraction of any new phase may be detectable even at room temperature. Cognizant of the slow creep in resistance over time seen in the 36 and 42 GPa loadings, diffraction was acquired within 3 days of the sample being retrieved from the cryostat assembly. Diffraction of post-transformed RuO_2 is shown in Fig. 7, and it includes contributions from the Al_2O_3 insulating mixture and platinum leads also present in the sample chamber. Given that the insulator-like behavior is more indicative of the fluorite-type phase than the HP-PdF_2-type phase, the aim was to verify which cubic structure was present in our sample. The diffraction data can be structurally refined using the Le Bail method to both $Pa\bar{3}$ and $Fm\bar{3}m$ phases, which is not unexpected. As mentioned earlier, the key crystallographic difference between the two cubic phases is the position of the oxygen atoms, which can make distinguishing between the two phases difficult when XRD is the probe. In both structures, the oxygens occupy an $8c$ (u, u, u) Wyckoff site with $u > 0.250$ in HP-PdF_2-type RuO_2 and $u = 0.250$ in fluorite-type RuO_2 [14,24]. Many $(hk\ell)$ reflections are common to the two structures, but the relative intensities of said reflections change based on Wyckoff positional coordinate u of the oxygen atoms. Our simulations typically yielded $u \sim 0.36$ for optimized HP-PdF_2-type structures in line with previous simulation

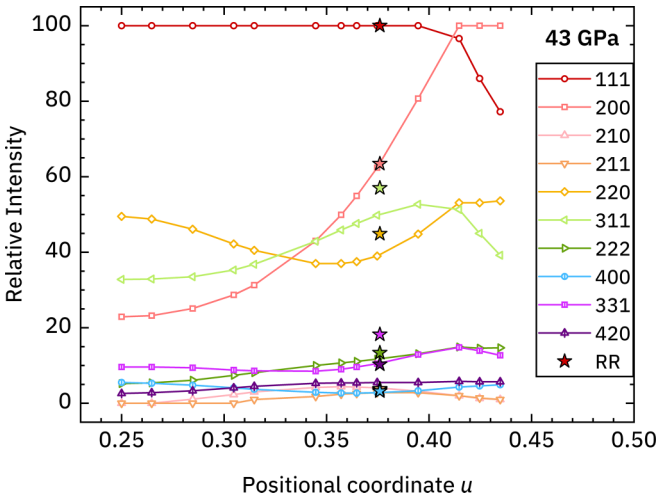

FIG. 8. Relative diffraction peak intensities of the HP-PdF_2-type structure as a function of Wyckoff 8c site coordinate u over the range of $0.25 < u < 0.435$, encompassing the values seen when comparing fluorite-type ($u = 0.25$) to HP-PdF_2-type structures. Intensities were calculated in VESTA with lattice parameters from the 43 GPa Rietveld refinement of Fig. 7. Star symbols ($\star$) at $u = 0.376$ represent the computed relative intensities extracted from that refinement as well, and indicate most agreement with an HP-PdF_2-type $Pa\bar{3}$ solution as compared to an $Fm\bar{3}m$-type solution.

studies [18,25,26]. Using VESTA software, we calculated the relative intensities of these $hk\ell$s for a simulated HP-PdF_2-type structure as a function of changing u (Fig. 8) ranging from the fluorite-type $u = 0.25$ to $u > 0.44$, which exceeds the u value range for HP-PdF_2-type structures [24,65]. A Rwp = 0.47% Rietveld refinement, shown in Fig. 7, finds greater agreement with the $Pa\bar{3}$ structure based on the relative intensities of peaks, with $V = 104.21(3)$ Å^3 and $u = 0.376(1)$. Platinum is refined as $a = 3.7745(2)$ Å and $V = 53.775(9)$ Å^3, which corresponds to approximately 43 GPa based on the Rose-Vinet universal EOS of Holmes *et al.* [43] as opposed to 56 GPa when determined with the Raman spectra of the diamond culet [37].

Throughout the latter half of the 20th century, the fluorite-type phase was considered a likely high-pressure polymorph for a great number of rutile-type dioxides including SnO_2, PbO_2, RuO_2, SiO_2, and even the archetypal rutile itself, TiO_2 [14,66–69]. Early XRD work on high-pressure phases of SnO_2, PbO_2, and RuO_2 discovered a common cubic structure that was ascribed as fluorite-type $Fm\bar{3}m$ phase [14,68,70]. However, Haines *et al.* [22] starting in 1996 showed this cubic phase to be in fact $Pa\bar{3}$, which led to questioning the $Fm\bar{3}m$ assignment in other metal dioxides. Since then, multitudinous XRD, neutron diffraction, and Raman studies have consistently found the presence of $Pa\bar{3}$ rather than $Fm\bar{3}m$ for SiO_2, RuO_2, SnO_2, and PbO_2 [24,58,71–74], although confusion understandably persists where $Pa\bar{3}$ is referred to as the fluorite-type phase [75–78]. Other cases, like TiO_2, have an experimentally known high-pressure cubic polymorph but have, to our knowledge, been unable to unambiguously determine between $Pa\bar{3}$ or $Fm\bar{3}m$ lattices [67,79–81]. More recent experiments claiming to find the $Fm\bar{3}m$ phase of these materials are exceedingly rare [82]. In cases like SiO_2, experimental and computational work indicates the $Fm\bar{3}m$ phase to be increasingly unlikely due to thermodynamic instability [72,83,84]. This is not the case universally, as many of these materials still have DFT predicted transition pathways to a high-pressure $Fm\bar{3}m$ phase [18,32,79,85–87], with an unfortunate dearth of experimental work to support them. While CaF_2-type metal dioxides are not unheard of—they are found in actinide dioxides such as AmO_2 and CmO_2 [88] and lanthanide dioxides such as CeO_2 [89]—finding this structure in the phase space of specifically a rutile-type precursor remains surprisingly elusive. This work is another example that seems to indicate that some barrier exists between DFT methods and experiment when it comes to revealing an $Fm\bar{3}m$ phase in these materials.

Our calculations of the temperature dependency between $Pa\bar{3}$ and $Fm\bar{3}m$ phases have interesting implications for RuO_2 prepared under different thermodynamic conditions. A different sample was prepared for XRD experiments by pressurizing to approximately 64 GPa and laser heating. The resulting XRD data contained a cubic phase that can be refined as the expected HP-PdF_2-type structure as well as a new, lower symmetry phase. The new phase was present throughout the powder sample, but phase fractions varied by location. The sample region where the intensities of the peaks belonging to the new phase were at their highest exhibited poor powder averaging overall, making Rietveld refinement of that data intractable. The integrated diffraction pattern from this region is shown in Fig. 9, and it was analyzed using the Le Bail method of structure refinement.

The multitude of peaks attributed to the new phase indicates a lower symmetry structure than either of the cubic HP-PdF_2-type or fluorite-type phases. Combining XRD structural refinement and computational methods, we tested many candidate structural archetypes known for AX_2 systems while trying to identify the new phase. This includes the same phases seeded into the crystal structure prediction simulations: marcasite, α-PbO_2, baddeleyite, arsenopyrite, monoclinic-VO_2, monoclinic-distorted rutile, and even a Pc lattice derived by relaxing the symmetry constraints of a $P2_1/c$ lattice [4,58–61]. None of these structures were more enthalpically favorable than the fluorite-type or HP-PdF_2-type structures (Fig. 5 and Ref. [56]) indicating that the lower symmetry phase is likely a metastable phase recovered from the nonequilibrium laser heating conditions. Of these candidate structures, the Pc and arsenopyrite-type $P2_1/c$ structures provided the best results in terms of Le Bail structural refinement to the diffraction data (detailed in [56]). Of these two structures, the Pc structure was significantly less enthalpically favorable compared to the arsenopyrite-type structure, which is the most enthalpically favorable of all the monoclinic candidates evaluated. As such, we tentatively ascribe the newly discovered phase as an arsenopyrite-type ($P2_1/c$) structure, which is a monoclinic distortion of the marcasite-type structure that is closely related to the $CaCl_2$-type structure [90–92]. Figure 5 shows that at this pressure, such a monoclinic distortion is more enthalpically favorable than its $CaCl_2$-type counterpart, which coexists with the HP-PdF_2 structure at pressures just below this measurement [14,17,58]. This assignment is not unique to this work, and it has been previously

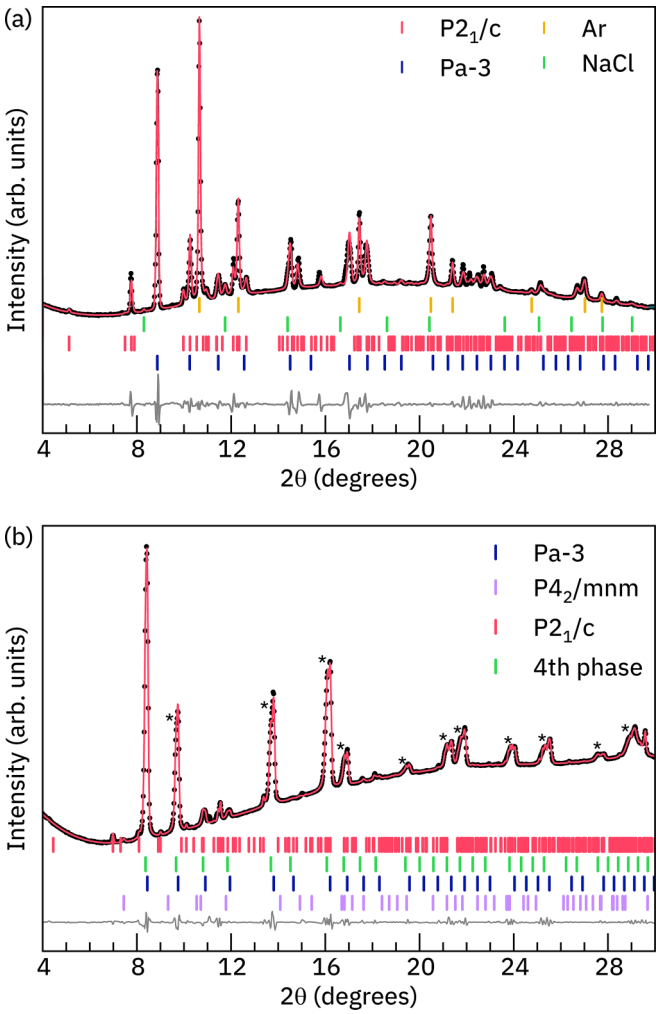

FIG. 9. (a) Le Bail refinement with multiple phases of RuO_2 present after laser heating and at 62 GPa. XRD featured here is from the sample region with the highest phase fraction of the tentatively assigned $P2_1/c$ phase. (b) Le Bail refinement of the same sample recovered after decompression at 0 GPa. We can see that the proportion of the $Pa\bar{3}$ phase is higher for this region and pressure. Asterisks mark peaks belonging to the "4th phase," which here was fit as a second $Pa\bar{3}$ structure of a larger volume.

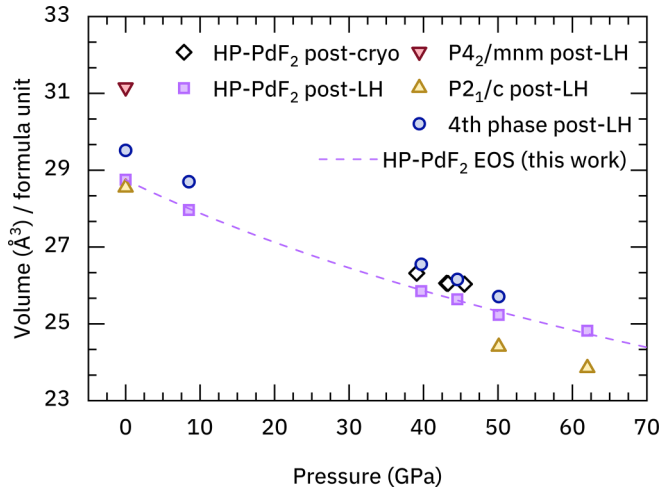

FIG. 10. Pressure-volume relationships obtained upon decompression for the four recovered phases from the laser-heated sample shown in Fig. 9, as well as for the HP-PdF_2-type phase in Fig. 7 measured following low-temperature experiments. Volumes were computed with Le Bail refinement of XRD acquired during decompression; errors in volumes are within the size of the symbol. The equation of state (as described in the text) for the HP-PdF_2-type phase recovered from the laser heating experiment is shown with a dashed line.

offered as a possibility for distortions seen in $CaCl_2$-type RuO_2 under pressure [14].

At 62 GPa, a Rwp = 1.62% Le Bail refinement returns a volume of 95.40(0) Å^3 for the arsenopyrite-type structure with lattice parameters $a = 5.28(2)$ Å, $b = 4.3347(8)$ Å, $c = 4.75(1)$ Å, and $\beta = 118.93(3)^\circ$. The refined lattice parameters of the HP-PdF_2-type $Pa\bar{3}$ phase are $a = 4.6305(4)$ Å and $V = 99.29(3)$ Å^3. In addition to the phases of RuO_2, the diffraction pattern of Fig. 9 also has contributions from the argon PTM and NaCl pellets that were incorporated in the sample chamber. These contributions are included in the refinement with argon in the $Fm\bar{3}m$ phase with $a = 3.8555(2)$ Å, and NaCl in the $Pm\bar{3}m$ phase with $a = 2.857(2)$ Å.

To confirm the cubic phase as HP-PdF_2-type $Pa\bar{3}$, a Rietveld refinement was performed from diffraction data in a sample region that had better powder statistics and a minimum amount of the additional phase. A Rwp = 1.81% Rietveld refinement of a HP-PdF_2-type structure to diffraction from this region returned lattice parameters $a = 4.6492(2)$ Å, $V = 100.49(1)$ Å^3, and anion position $u = 0.3618(6)$. The calculated relative intensities for this structure were also plotted in a similar fashion as in Fig. 8 (included in [56]) and show good agreement with behavior expected for $Pa\bar{3}$ RuO_2.

The post-laser heated sample was decompressed to 0 GPa, and XRD of the recovered sample includes the HP-PdF_2-type and arsenopyrite-type structures in addition to other peaks that were not present at 62 GPa, shown in Fig. 9. A Le Bail refinement, Rwp = 0.64% to the HP-PdF_2-type and arsenopyrite-type phases, returns $V = 115.00(1)$ and 114.20(1) Å^3, respectively, with the volume of decompressed HP-PdF_2-type RuO_2 in good agreement with previous reports [14,17,35]. Some of the new peaks present can be attributed to the rutile-type structure, $P4_2/mnm$, which other studies have found upon decompression as well [14,35]. Our refinement with the rutile-type phase returns a volume of $V = 62.4(2)$ Å^3, which is in good agreement with reported values for ambient RuO_2 [14,17,56]. The other additional peaks seen upon decompression are evident in the broadening and splitting of the $Pa\bar{3}$ peaks. The Debye-Scherrer rings of these peaks are smoother than the spotty rings assigned to the HP-PdF_2-type RuO_2 (image in [56]). We found that no single phase could account for all the multiple peaks overlapping in the HP-PdF_2-type pattern. This led us to treat the closely situated and overlapping features as the original HP-PdF_2-type structure with an additional, similar phase that either formed or became more pronounced upon decompression. These peaks, called the "fourth phase" in Figs. 9 and 10, can be successfully fitted with Le Bail and Rietveld methods as a second $Pa\bar{3}$ phase or as a lower symmetry, $Pbca$, orthorhombically distorted HP-PdF_2-type phase. Such an orthorhombic phase

has been seen or predicted in some HP-PdF_2-type metal difluorides during decompression from high pressures [93–95]. While refinements of the *Pbca* structure provide reasonable results, DFT optimizations of that structure between 0 and 66 GPa resort to the $Pa\bar{3}$ structure. The CSP generated $Pbc2_1$ and $C2/m$ phases, as well as fluorite-type RuO_2 and common orthorhombic MO_2 phases of α-PbO_2-type and orthorhombic ZrO_2-type (i.e., SrI_2-type) phases, were also tested but did not provide better solutions compared to either *Pbca* or $Pa\bar{3}$ structures (see the Supplemental Material [56]). Therefore, without additional data we are inclined to assign this "fourth phase" as a second, more strained, finer-grained HP-PdF_2-type phase in the sample that possibly arose due to inhomogeneities in the laser heating.

Unit-cell volumes of multiple RuO_2 phases in the post-laser-heated RuO_2 sample are plotted as a function of pressure, in addition to volumes of the $Pa\bar{3}$ phase from the 60 GPa series post-cryostat XRD experiment, in Fig. 10. These data were acquired during decompression. A second-order Birch-Murnaghan EOS is fitted to the HP-PdF_2-type structure using $V_0 = 115.0$ Å^3 and B_0' constrained to equal 4. The fitted bulk modulus is found to be $B = 306(4)$ GPa. This is less than previously reported when the $Pa\bar{3}$ phase was initially characterized, but more than other subsequent experimental studies [14,17,22].

In addition to its absence in the post-cryostat XRD, the density of states (Fig. 6) of arsenopyrite-type RuO_2 shows that the phase is metallic in nature. This supports that arsenopyrite-type RuO_2 is not responsible for the low-temperature, high-pressure electronic transition observed in our electrical resistance measurements. We also do not detect with XRD the presence of the $Fm\bar{3}m$ phase in either post-cryostat or post-laser-heated samples. In the latter case, this is not unexpected based on the conclusion from our simulations that the fluorite-type phase could be preferable at low temperatures in this pressure region. By compressing at room temperature and laser heating, we ensured that the sample environment was most favorable to the formation of the HP-PdF_2-type phase. For the post-cryostat sample, we expect the phase fraction of $Fm\bar{3}m$ RuO_2, if present, to be maximized while at low temperature. If the observed loss of metallicity is indeed caused by the emergence of the fluorite-type phase at low temperature and high pressure, it could be that the fraction remaining in our room-temperature sample could not be distinguished from the majority HP-PdF_2-type phase.

IV. CONCLUSIONS

We performed electrical transport measurements at high pressures and low temperatures, revealing a loss in metallicity in RuO_2 above 28 GPa. We found that such a change in electronic behavior could not be attributed to any previously established phase of RuO_2, i.e., rutile-type, $CaCl_2$-type, or HP-PdF_2-type. In addition, the low-temperature resistance behavior of $CaCl_2$-type and HP-PdF_2-type phases at 16 and 28 GPa agrees with electronic structure calculations, which predict the phases to be metallic. The only simulated phase identified in this work that exhibits insulative behavior is the fluorite-type phase. However, this phase was not detected in room-temperature XRD of a sample that had undergone low-temperature cycling. Powder x-ray diffraction measurements of a separate sample after laser-heating at 64 GPa revealed the coexistence of the HP-PdF_2-type phase and a new monoclinic phase, which we view as a distortion of the closely related $CaCl_2$-type structure and assign as the arsenopyrite-type phase. DFT calculations predict this arsenopyrite-type phase to be metallic.

ACKNOWLEDGMENTS

This material is based upon work supported by the Air Force Office of Scientific Research under Award No. FA9550-21-1-0097. Portions of this work were performed at HPCAT (Sector 16), Advanced Photon Source (APS), Argonne National Laboratory. HPCAT operations are supported by DOE-NNSA's Office of Experimental Sciences. The Advanced Photon Source is a U.S. Department of Energy (DOE) Office of Science User Facility operated for the DOE Office of Science by Argonne National Laboratory under Contract No. DE-AC02-06CH11357. The authors would like to thank the UNLV National Supercomputing Institute for computational resources and support, and Paul Ellison for assistance with gas loading.

[1] J. D. Dunitz and L. E. Orgel, Electronic properties of transition-metal oxides-I: Distortions from cubic symmetry, J. Phys. Chem. Solids **3**, 20 (1957).

[2] D. Adler, Mechanisms for metal-nonmental transitions in transition-metal oxides and sulfides, Rev. Mod. Phys. **40**, 714 (1968).

[3] A. O'Hara and A. A. Demkov, Nature of the metal-insulator transition in NbO_2, Phys. Rev. B **91**, 094305 (2015).

[4] Z. Hiroi, Structural instability of the rutile compounds and its relevance to the metal-insulator transition of VO_2, Prog. Solid State Chem. **43**, 47 (2015).

[5] J. H. Park, J. M. Coy, T. S. Kasirga, C. Huang, Z. Fei, S. Hunter, and D. H. Cobden, Measurement of a solid-state triple point at the metal-insulator transition in VO_2, Nature (London) **500**, 431 (2013).

[6] D. Adler, Electrical and optical properties of transition-metal oxides, Radiat. Eff. **4**, 123 (1970).

[7] F. Aguilera-Granja and A. Ayuela, Magnetism and distortions in two-dimensional transition-metal dioxides: On the quest for intrinsic magnetic semiconductor layers, J. Phys. Chem. C **124**, 2634 (2020).

[8] H. Over, Surface chemistry of ruthenium dioxide in heterogeneous catalysis and electrocatalysis: From fundamental to applied research, Chem. Rev. **112**, 3356 (2012).

[9] Y. Qin, T. Yu, S. Deng, X.-Y. Zhou, D. Lin, Q. Zhang, Z. Jin, D. Zhang, Y.-B. He, H.-J. Qiu, L. He, F. Kang, K. Li, and T.-Y. Zhang, RuO_2 electronic structure and lattice strain dual engineering for enhanced acidic oxygen evolution reaction performance, Nat. Commun. **13**, 3784 (2022).

[10] M. Uchida, T. Nomoto, M. Musashi, R. Arita, and M. Kawasaki, Superconductivity in uniquely strained RuO_2 films, Phys. Rev. Lett. **125**, 147001 (2020).

[11] M. S. Osofsky, C. M. Krowne, K. M. Charipar, K. Bussmann, C. N. Chervin, I. R. Pala, and D. R. Rolison, Disordered RuO_2 exhibits two dimensional, low-mobility transport and a metal-insulator transition, Sci. Rep. **6**, 21836 (2016).

[12] D.-S. Ko *et al.*, Understanding the structural, electrical, and optical properties of monolayer h-phase RuO_2 nanosheets: a combined experimental and computational study, NPG Asia Mater **10**, 266 (2018).

[13] S. Biswas, First-principles investigation of the metal-insulator transition in rutile RuO_2, Thin Solid Films **736**, 138925 (2021).

[14] J. Haines and J. M. Léger, Phase transitions in ruthenium dioxide up to 40 GPa: Mechanism for the rutile-to-fluorite phase transformation and a model for the high-pressure behavior of stishovite SiO_2, Phys. Rev. B **48**, 13344 (1993).

[15] S. S. Rosenblum, W. H. Weber, and B. L. Chamberland, Raman-scattering observation of the rutile-to-$CaCl_2$ phase transition in RuO_2, Phys. Rev. B **56**, 529 (1997).

[16] S. Ono and K. Mibe, Determination of the phase boundary of the ferroelastic rutile to $CaCl_2$ transition in RuO_2 using *in situ* high-pressure and high-temperature Raman spectroscopy, Phys. Rev. B **84**, 054114 (2011).

[17] K. Armstrong, N. C. Siersch, T. Boffa-Ballaran, D. J. Frost, T. Yu, and Y. Wang, Equations of state, phase relations, and oxygen fugacity of the Ru-RuO_2 buffer at high pressures and temperatures, Am. Mineral. **105**, 333 (2020).

[18] R. Ahuja, S. Rekhi, S. Saxena, and B. Johansson, High-pressure structural phase transitions in RuO_2 and its geophysical implications, J. Phys. Chem. Solids **62**, 2035 (2001).

[19] D. Smith, D. Sneed, N. Dasenbrock-Gammon, E. Snider, G. A. Smith, C. Childs, J. S. Pigott, N. Velisavljevic, C. Park, K. V. Lawler, R. P. Dias, and A. Salamat, Anomalous conductivity in the rutile structure driven by local disorder, J. Phys. Chem. Lett. **10**, 5351 (2019).

[20] G. A. Smith, D. Schacher, J. K. Hinton, D. Sneed, C. Park, S. Petitgirard, K. V. Lawler, and A. Salamat, Prevalence of pretransition disordering in the rutile-to- $CaCl_2$ phase transition of GeO_2, Phys. Rev. B **104**, 134107 (2021).

[21] J. Haines, J. M. Léger, O. Schulte, and S. Hull, Neutron diffraction study of the ambient-pressure, rutile-type and the high-pressure, $CaCl_2$-Type Phases of Ruthenium Dioxide, Acta Crystallogr. B: Struct. Sci. **53**, 880 (1997).

[22] J. Haines, J. M. Léger, and O. Schulte, $Pa\bar{3}$ Modified fluorite-type structures in metal dioxides at high pressure, Science **271**, 629 (1996).

[23] J. M. Léger, J. Haines, A. Atouf, and P. Tomaszewski, Phase transitions in several metal dioxides as studied by angle dispersive x-ray diffraction up to 50 GPa, in *AIP Conference Proceedings, Colorado Springs, CO* (AIP, New York, 1994), Vol. 309, pp. 363–366.

[24] J. Haines, J. M. Léger, M. W. Schmidt, J. P. Petitet, A. S. Pereira, J. A. H. Da Jornada, and S. Hull, Structural characterisation of the $Pa\bar{3}$-type, high pressure phase of ruthenium dioxide, J. Phys. Chem. Solids **59**, 239 (1998).

[25] V. Maurya, G. Sharma, and K. B. Joshi, First-principles characterisation of structural and electronic properties of some RuO_2 crystals, Phys. Scr. **96**, 055807 (2021).

[26] N. Mehtougui, D. Rached, R. Khenata, H. Rached, M. Rabah, and S. Bin-Omran, Structural, electronic and mechanical properties of RuO_2 from first-principles calculations, Mater. Sci. Semicond. Proc. **15**, 331 (2012).

[27] A. Tressaud, J. L. Soubeyroux, H. Touhara, G. Demazeau, and F. Langlais, On a new structural type of fluorine compounds: Crystal and magnetic structures of a high pressure form of PdF_2, Mater. Res. Bull. **16**, 207 (1981).

[28] J. Haines, J. M. Léger, F. Gorelli, D. D. Klug, J. S. Tse, and Z. Q. Li, X-ray diffraction and theoretical studies of the high-pressure structures and phase transitions in magnesium fluoride, Phys. Rev. B **64**, 134110 (2001).

[29] D. Vrel, J.-P. Petitet, X. Huang, and T. Mashimo, Synthesis of ruthenium oxide high pressure phases by shock compression, Phys. B: Condens. Matter **239**, 9 (1997).

[30] J. M. Léger, J. Haines, and B. Blanzat, Materials potentially harder than diamond: Quenchable high-pressure phases of transition metal dioxides, J. Mater. Sci. Lett. **13**, 1688 (1994).

[31] J. M. Léger, P. Djemia, F. Ganot, J. Haines, A. S. Pereira, and J. A. H. da Jornada, Hardness and elasticity in cubic ruthenium dioxide, Appl. Phys. Lett. **79**, 2169 (2001).

[32] J. S. Tse, D. D. Klug, K. Uehara, Z. Q. Li, J. Haines, and J. M. Léger, Elastic properties of potential superhard phases of RuO_2, Phys. Rev. B **61**, 10029 (2000).

[33] J. Riga, C. Tenret-Noël, J. J. Pireaux, R. Caudano, J. J. Verbist, and Y. Gobillon, Electronic structure of rutile oxides TiO_2, RuO_2 and IrO_2 studied by x-ray photoelectron spectroscopy, Phys. Scr. **16**, 351 (1977).

[34] J. J. Lin, S. M. Huang, Y. H. Lin, T. C. Lee, H. Liu, X. X. Zhang, R. S. Chen, and Y. S. Huang, Low temperature electrical transport properties of RuO_2 and IrO_2 single crystals, J. Phys.: Condens. Matter **16**, 8035 (2004).

[35] Y. Shirako, X. Wang, Y. Tsujimoto, K. Tanaka, Y. Guo, Y. Matsushita, Y. Nemoto, Y. Katsuya, Y. Shi, D. Mori, H. Kojitani, K. Yamaura, Y. Inaguma, and M. Akaogi, Synthesis, crystal structure, and electronic properties of high-pressure PdF_2-Type Oxides MO_2 (M = Ru, Rh, Os, Ir, Pt), Inorg. Chem. **53**, 11616 (2014).

[36] G. Shen, Y. Wang, A. Dewaele, C. Wu, D. E. Fratanduono, J. Eggert, S. Klotz, K. F. Dziubek, P. Loubeyre, O. V. Fat'yanov, P. D. Asimow, T. Mashimo, R. M. M. Wentzcovitch, and other members of the IPPS task group, Toward an international practical pressure scale: A proposal for an IPPS ruby gauge (IPPS-Ruby2020), High Press. Res. **40**, 299 (2020).

[37] Y. Akahama and H. Kawamura, High-pressure Raman spectroscopy of diamond anvils to 250 GPa: Method for pressure determination in the multimegabar pressure range, J. Appl. Phys. **96**, 3748 (2004).

[38] Y. Feng, R. Jaramillo, J. Wang, Y. Ren, and T. F. Rosenbaum, Invited Article: High-pressure techniques for condensed matter physics at low temperature, Rev. Sci. Instrum. **81**, 041301 (2010).

[39] F. Datchi, A. Dewaele, P. Loubeyre, R. Letoullec, Y. Le Godec, and B. Canny, Optical pressure sensors for high-pressure - high-temperature studies in a diamond anvil cell, High Press. Res. **27**, 447 (2007).

[40] K. Nakano, Y. Akahama, Y. Ohishi, and H. Kawamura, Ruby scale at low temperatures calibrated by the NaCl gauge: Wavelength shift of ruby R1 fluorescence line at high pressure and low temperature, Jpn. J. Appl. Phys. **39**, 1249 (2000).

[41] H. Yamaoka, Y. Zekko, I. Jarrige, J.-F. Lin, N. Hiraoka, H. Ishii, K.-D. Tsuei, and J. Mizuki, Ruby pressure scale in a low-temperature diamond anvil cell, J. Appl. Phys. **112**, 124503 (2012).

[42] D. Smith, D. P. Shelton, P. B. Ellison, and A. Salamat, Simple imaging for the diamond anvil cell: Applications to hard-to-reach places, Rev. Sci. Instrum. **89**, 103902 (2018).

[43] N. C. Holmes, J. A. Moriarty, G. R. Gathers, and W. J. Nellis, The equation of state of platinum to 660 GPa (6.6 Mbar), J. Appl. Phys. **66**, 2962 (1989).

[44] A. Dewaele, A. D. Rosa, N. Guignot, D. Andrault, J. E. F. S. Rodrigues, and G. Garbarino, Stability and equation of state of face-centered cubic and hexagonal close packed phases of argon under pressure, Sci. Rep. **11**, 15192 (2021).

[45] C. Prescher and V. B. Prakapenka, DIOPTAS: a program for reduction of two-dimensional x-ray diffraction data and data exploration, High Press. Res. **35**, 223 (2015).

[46] B. H. Toby and R. B. Von Dreele, GSAS-II: the genesis of a modern open-source all purpose crystallography software package, J. Appl. Crystallog. **46**, 544 (2013).

[47] A. Togo and I. Tanaka, First principles phonon calculations in materials science, Scr. Mater. **108**, 1 (2015).

[48] A. Togo, First-principles phonon calculations with phonopy and phono3py, J. Phys. Soc. Jpn. **92**, 012001 (2023).

[49] J. Sun, A. Ruzsinszky, and J. P. Perdew, Strongly constrained and appropriately normed semilocal density functional, Phys. Rev. Lett. **115**, 036402 (2015).

[50] H. J. Monkhorst and J. D. Pack, Special points for brillouin-zone integrations, Phys. Rev. B **13**, 5188 (1976).

[51] P. E. Blöchl, Projector augmented-wave method, Phys. Rev. B **50**, 17953 (1994).

[52] A. R. Oganov and C. W. Glass, Crystal structure prediction using ab initio evolutionary techniques: Principles and applications, J. Chem. Phys. **124**, 244704 (2006).

[53] A. R. Oganov, A. O. Lyakhov, and M. Valle, How evolutionary crystal structure prediction works-and why, Acc. Chem. Res. **44**, 227 (2011).

[54] A. O. Lyakhov, A. R. Oganov, H. T. Stokes, and Q. Zhu, New developments in evolutionary structure prediction algorithm USPEX, Comput. Phys. Commun. **184**, 1172 (2013).

[55] K. Kannan and B. L. Yang, Metal-to-semimetal transition in platinum nanotubes: Dependence on thickness, J. Phys. Chem. Lett. **12**, 2183 (2021).

[56] See Supplemental Material at http://link.aps.org/supplemental/10.1103/PhysRevMaterials.8.013603. for more details of electrical transport measurements, additional XRD data and analysis, and additional electronic band structure, enthalpy, DOS, and ELF computation results for high-pressure phases of RuO_2.

[57] A. K. Goel, G. Skorinko, and F. H. Pollak, Optical properties of single-crystal rutile RuO_2 and IrO_2 in the range 0.5 to 9.5 eV, Phys. Rev. B **24**, 7342 (1981).

[58] J. Haines, J. M. Léger, and O. Schulte, The high-pressure phase transition sequence from the rutile-type through to the cotunnite-type structure in PbO_2, J. Phys.: Condens. Matter **8**, 1631 (1996).

[59] J. M. Longo, P. Kierkegaard, C. J. Ballhausen, U. Ragnarsson, S. E. Rasmussen, E. Sunde, and N. A. Sørensen, A Refinement of the Structure of VO_2., Acta Chem. Scand. **24**, 420 (1970).

[60] B. G. Brandt, On the crystal structures of MoO_2 and $MoO_3(H_2O)_2$: An account of computer programming and structure refinement, Chemical Communications (University of Stockholm, 1971), Vol. 9.

[61] H. P. S. Corrêa, I. P. Cavalcante, L. G. Martinez, C. G. P. Orlando, and M. T. D. Orlando, Refinement of monoclinic ReO_2 structure from XRD by Rietveld method, Braz. J. Phys. **34**, 1208 (2004).

[62] S. López-Moreno, A. H. Romero, J. Mejía-López, and A. Muñoz, First-principles study of pressure-induced structural phase transitions in MnF_2, Phys. Chem. Chem. Phys. **18**, 33250 (2016).

[63] T. Berlijn, *et al.*, Itinerant antiferromagnetism in RuO_2, Phys. Rev. Lett. **118**, 077201 (2017).

[64] S. L. Dudarev, G. A. Botton, S. Y. Savrasov, C. J. Humphreys, and A. P. Sutton, Electron-energy-loss spectra and the structural stability of nickel oxide: An LSDA+U study, Phys. Rev. B **57**, 1505 (1998).

[65] K. Momma and F. Izumi, VESTA 3 for three-dimensional visualization of crystal, volumetric and morphology data, J. Appl. Cryst. **44**, 1272 (2011).

[66] Y. Syono and S. Akimoto, High pressure synthesis of fluorite-type PbO_2, Mater. Res. Bull. **3**, 153 (1968).

[67] K. Kusaba, M. Kikuchi, K. Fukuoka, and Y. Syono, Anisotropic phase transition of rutile under shock compression, Phys. Chem. Miner. **15**, 238 (1988).

[68] L.-G. Liu, A fluorite isotype of SnO_2 and a new modification of TiO_2: Implications for the earth's lower mantle, Science **199**, 422 (1978).

[69] Y. Tsuchida and T. Yagi, A new, post-stishovite highpressure polymorph of silica, Nature (London) **340**, 217 (1989).

[70] T. Yagi and S.-I. Akimoto, Phase boundary and transition rate of orthorhombic-cubic transformation in PbO_2, J. Geophys. Res.: Solid Earth **85**, 6991 (1980).

[71] J. Haines and J. M. Léger, X-ray diffraction study of the phase transitions and structural evolution of tin dioxide at high pressure: Relationships between structure types and implications for other rutile-type dioxides, Phys. Rev. B **55**, 11144 (1997).

[72] Y. Kuwayama, K. Hirose, N. Sata, and Y. Ohishi, Pressure-induced structural evolution of pyrite-type SiO_2, Phys. Chem. Miner. **38**, 591 (2011).

[73] S. Ono, E. Ito, T. Katsura, A. Yoneda, M. J. Walter, S. Urakawa, W. Utsumi, and K. Funakoshi, Thermoelastic properties of the high-pressure phase of SnO_2 determined by in situ x-ray observations up to 30 GPa and 1400 K, Phys. Chem. Miner. **27**, 618 (2000).

[74] B. Grocholski, S.-H. Shim, E. Cottrell, and V. B. Prakapenka, Crystal structure and compressibility of lead dioxide up to 140 GPa, Am. Mineral. **99**, 170 (2014).

[75] T. Ji, Y. Gao, D. Yue, W. Shen, Y. Yan, and Y. Han, Fluorite phase transition in SnO_2 under uniaxial compression and at 500 K, J. Phys. Chem. C **123**, 5603 (2019).

[76] Y. He, J. F. Liu, W. Chen, Y. Wang, H. Wang, Y. W. Zeng, G. Q. Zhang, L. N. Wang, J. Liu, T. D. Hu, H. Hahn, H. Gleiter, and J. Z. Jiang, High-pressure behavior of SnO_2 nanocrystals, Phys. Rev. B **72**, 212102 (2005).

[77] Z. Dong and Y. Song, Pressure-induced morphology-dependent phase transformations of nanostructured tin dioxide, Chem. Phys. Lett. **480**, 90 (2009).

[78] H. J. Gwon, N.-R. Kang, Y. Lee, S. O. Won, H. J. Chang, J.-W. Choi, C.-Y. Kang, S. K. Kim, B. Kwon, S. Nahm, J.-Y. Kim, J.-S. Kim, and S.-H. Baek, Enhancement of mechanical hardness in SnO_xN_y with a dense high-pressure cubic phase of SnO_2, Chem. Mater. **28**, 7051 (2016).

[79] D. Y. Kim, J. S. de Almeida, L. Koci, and R. Ahuja, Dynamical stability of the hardest known oxide and the cubic solar material: TiO_2, Appl. Phys. Lett. **90**, 171903 (2007).

[80] M. Mattesini, J. S. de Almeida, L. Dubrovinsky, N. Dubrovinskaia, B. Johansson, and R. Ahuja, High-pressure and high-temperature synthesis of the cubic TiO_2 polymorph, Phys. Rev. B **70**, 212101 (2004).

[81] D. Dash and S. Chaudhury, A density functional theory based analysis on the electronic, mechanical, and optical properties of cubic TiO_2, Mater. Today: Proc.Int. Nanotechnol.**18**, 596 (2019).

[82] J. Z. Jiang, L. Gerward, and J. S. Olsen, Pressure induced phase transformation in nanocrystal SnO_2, Scr. Mater. **44**, 1983 (2001).

[83] A. R. Oganov, M. J. Gillan, and G. D. Price, Structural stability of silica at high pressures and temperatures, Phys. Rev. B **71**, 064104 (2005).

[84] K. Taeck Park, K. Terakura, and Y. Matsui, Theoretical evidence for a new ultra-high-pressure phase of SiO_2, Nature (London) **336**, 670 (1988).

[85] I. Erdem, H. H. Kart, and T. Cagin, High pressure phase transitions in SnO_2 polymorphs by first-principles calculations, J. Alloys Compd. **587**, 638 (2014).

[86] F. El Haj Hassan, S. Moussawi, W. Noun, C. Salameh, and A. V. Postnikov, Theoretical calculations of the high-pressure phases of SnO_2, Comput. Mater. Sci. **72**, 86 (2013).

[87] Q.-J. Liu, Z. Ran, F.-S. Liu, and Z.-T. Liu, Phase transitions and mechanical stability of TiO_2 polymorphs under high pressure, J. Alloys Compd. **631**, 192 (2015).

[88] J. Dancausse, R. Haire, S. Heathman, and U. Benedict, High-pressure x-ray diffraction studies of americium and curium dioxides, J. Nucl. Sci. Technol. **39**, 136 (2002).

[89] M. K. Jacobsen, N. Velisavljevic, D. M. Dattelbaum, R. S. Chellappa, and C. Park, High pressure and temperature equation of state and spectroscopic study of CeO_2, J. Phys.: Condens. Matter **28**, 155401 (2016).

[90] J. A. Tossell, D. J. Vaughan, and J. K. Burdett, Pyrite, marcasite, and arsenopyrite type minerals: Crystal chemical and structural principles, Phys. Chem. Miner. **7**, 177 (1981).

[91] S. D. Wijeyesekera and R. Hoffmann, Marcasite and arsenopyrite: structure, bonding, and electrical properties, Inorg. Chem. **22**, 3287 (1983).

[92] B. G. Hyde, The effect of non-bonded, anion-anion interactions on the $CaCl_2$/rutile transformation and on the bond lengths in the rutile type, Z. Krist. Cryst. Mater. **179**, 205 (1987).

[93] J. A. Barreda-Argüeso, S. López-Moreno, M. N. Sanz-Ortiz, F. Aguado, R. Valiente, J. González, F. Rodríguez, A. H. Romero, A. Muñoz, L. Nataf, and F. Baudelet, Pressure-induced phase-transition sequence in CoF_2: An experimental and first-principles study on the crystal, vibrational, and electronic properties, Phys. Rev. B **88**, 214108 (2013).

[94] E. Stavrou, Y. Yao, A. F. Goncharov, Z. Konôpková, and C. Raptis, High-pressure structural study of MnF_2, Phys. Rev. B **93**, 054101 (2016).

[95] U. Muller, *Symmetry Relationships between Crystal Structures: Applications of Crystallographic Group Theory in Crystal Chemistry*, International Union of Crystallography Texts on Crystallography (Oxford University Press, Oxford, 2013).